Engineered Science
DOI: https://dx.doi.org/10.30919/es923

Prediction of Undrained Lateral Capacity of Free-Head Rectangular Pile in Clay Using Finite Element Limit Analysis and Artificial Neural Network

Suttikarn Panomchaivath,[1] Wittaya Jitchaijaroen,[1] Rungkhun Banyong,[1] Suraparb Keawsawasvong,[1,*] Sayan Sirimontree[1] and Pitthaya Jamsawang[2]

Abstract

This paper is dedicated to investigating the undrained lateral capacity of rigid free-head rectangular/square piles in cohesive soil. The study utilizes the three-dimensional Finite Element Limit Analysis (FELA) framework to analyze and assess the pile's ability to withstand lateral loads. Both upper bound (UB) and lower bound (LB) FELA techniques are employed in the analysis process. The findings emphasize the importance of understanding the behavior and failure mechanisms exhibited by the surrounding soil around the pile. The analysis employs dimensionless approaches to obtain the normalized load factor, which represents the outcomes of the solution. The results obtained from the analysis demonstrate that the lateral load capacity of the soil is influenced by several key factors, including the pile's length-width ratio, the height-width ratio, the eccentricity of the lateral load, and the overburden stress where the discussion regarding the effects of all parameters is provided in the manuscript. The study also delves into the examination and understanding of the failure mechanisms exhibited by the soil in the context of lateral loaded piles. Based on the numerical outcome, the artificial neural network (ANN), which is one of soft-computing techniques, is utilized to establish a surrogate model for predicting the lateral capacity of rectangular piles. By considering these factors in the design process, engineers can make informed decisions that effectively optimize pile performance and ensure the long-term stability of structures.

Keywords: Lateral capacity; Rectangular pile; FELA; ANN; Soft-computing.
Received: 20 January 2023; Revised: 02 July 2023; Accepted: 04 July 2023.
Article type: Research article.

1. Introduction

Piles serve a wide range of applications in various industries. They are commonly used in building and infrastructure construction to provide structural support and transfer loads to stable soil or rock layers.[1-6] Pile foundations are crucial for deep foundation systems when shallow foundations are inadequate. Piles also play a significant role in marine structures, retaining walls, slope stability, and supporting energy and telecommunication structures. Moreover, piles are utilized in geotechnical investigations to assess soil conditions and gather valuable data. The specific use of piles depends on project requirements, site conditions, and the type of structure being built. Proper pile design and installation involve careful consideration of factors such as soil properties, structural loads, and environmental conditions to ensure the safety and efficiency of foundation systems.

Additionally, a pile is subjected to a lateral load, it experiences forces perpendicular to its longitudinal axis. The magnitude of the lateral load is determined by design requirements, structural characteristics, soil conditions, and environmental factors. The lateral load induces bending and shear stresses in the pile. To analyze and design piles for lateral loads, engineers consider the load magnitude, soil properties, pile stiffness, pile group effects, and utilize various analysis methods such as the p-y curve method, finite element analysis (FEA), and empirical approaches. Soil investigations and

[1] *Research Unit in Sciences and Innovative Technologies for Civil Engineering Infrastructures, Department of Civil Engineering, Faculty of Engineering, Thammasat School of Engineering, Thammasat University, Pathumthani 12120, Thailand.*
[2] *Soil Engineering Research Center, Department of Civil Engineering, King Mongkut's University of Technology North Bangkok, Bangkok 10800, Thailand.*
**Email:* ksurapar@engr.tu.ac.th (S. Keawsawasvong)

testing are conducted to gather relevant soil parameters. The design process involves ensuring equilibrium, compatibility, and strength requirements are met, taking into account the behavior of the soil-pile system. Designing piles for lateral loads is a complex task that necessitates geotechnical expertise and adherence to applicable design codes and standards to ensure the stability and safety of the foundation system. Broms[7] initially introduced a study on the lateral capacity of piles in clay by proposing an empirical approach. The approach used by Broms[7] involved the Limit Equilibrium Method (LEM), where assumptions were made about the earth pressure distributions along the length of the pile. By solving a set of equilibrium equations, Broms provided solutions for lateral piles in clay. Developing upon Broms' work, Meyerhof *et al*.[8] and Georgiadis *et al*.[9] further developed LEM schemes to offer new solutions for determining the lateral capacity of piles. These advancements took into consideration additional factors such as layered soils and sloping ground. Consequently, the new solutions incorporated improved earth pressure distributions along the length of the pile, accounting for the effects of different soil layers and sloping terrain.

Over the last four decades, multiple researchers have conducted studies on the lateral capacity of circular piles. For instance, Al-abboodi and Sabbagh,[10] Conte *et al*.,[11] Georgiadis,[12] Georgiadis and Georgiadis,[13] Keawsawasvong,[14] Keawsawasvong and Ukritchon,[15] and Zhang *et al*.[16] employed the conventional displacement-based finite element method (FEM) to investigate the maximum lateral load of circular piles in three-dimensional conditions. Other researchers, such as Yu *et al*.[17,18] Klar and Randolph,[19] and Murff and Hamilton,[20] utilized the limit analysis technique based on the upper bound (UB) and lower bound (LB) theorem to examine the lateral capacity of circular piles. Izadi and Chenari[21,22] employed the finite element limit analysis (FELA) approach to evaluate the ultimate lateral capacity of three-dimensional circular piles in clays. Regarding rectangular piles, Keawsawasvong and Ukritchon[23,24] and Ukritchon and Keawsawasvong[25] investigated the soil resistance under full-flow conditions around the mechanism for two-dimensional rectangular piles under plane strain conditions. The most up-to-date studies on fixed-head rectangular and circular piles under lateral resistance were performed by Keawsawasvong *et al.*.[26] They have investigated the undrained lateral resistance of fixed-headed rectangular and circular piles using FELA. However, there was no limit analysis solution for free-headed rectangular piles the past.

To the best of our knowledge, previous studies have primarily focused on the lateral capacity of three-dimensional (3D) circular piles or two-dimensional (2D) rectangular piles. Studies on three-dimensional rectangular free-head piles are notably limited. This paper focuses on providing limit state solutions for the lateral capacity of free-head rectangular piles in cohesive soils. It takes into account factors such as soil weight, the no-tension condition at the pile interface, pile length ratio, load eccentricity, and aspect ratio of rectangular shapes. The rectangular piles considered in the study are free-headed and subjected to lateral forces. To analyze soil behavior, the authors utilize the 3D finite element limit analysis (FELA) numerical technique. The study includes both upper bound (UB) and lower bound (LB) FELA solutions. The results obtained from the analysis are presented in the form of design charts. Moreover, the design charts show the numerical findings and provide valuable information on the undrained lateral capacity of free-headed rectangular piles. The charts also highlight the influence of factors such as soil weight and aspect ratio on the selected failure mechanisms. In addition, this study integrates an artificial neural network (ANN) and FELA approaches to create a cutting-edge model for rapidly and precisely estimating the undrained lateral capacity of free-headed rectangular piles. The presented ANN model is intended to assist practitioners as a black-box-type prediction model for practitioners to estimate the lateral behavior of such piles in their design and engineering projects.

Thus, the highlights of this paper are as follows:

1. The paper is the first study to focus on investigating the undrained lateral capacity of rigid free-head rectangular/square piles in cohesive soil using the three-dimensional Finite Element Limit Analysis (FELA) framework.
2. This article examines the influences on various factors on the lateral pile capacity such as the pile's length-width ratio, height-width ratio, eccentricity of the lateral load, and overburden stress.
3. An artificial neural network (ANN) is used to establish a surrogate model for predicting the lateral capacity of rectangular piles for the first time.

2. Problem formulation

Figure 1 illustrates the geometric configuration of a three-dimensional (3D) free-head rectangular pile model. The rigid pile experiences a horizontal force of P and, given the symmetric characteristics of the monotonically and laterally loaded pile scenario, only half of the model is employed in the simulation. The pile is considered completely rigid, and its cross section has a width (B), height (H), and length (L). Please note that, in Figure 1, the height of the pile's cross-section is $H/2$, reflecting the symmetrical condition is applied in the 3D

FELA analysis. Based on the assumption of a completely rough interface between the soil mass and the pile, the undrained shear strength at the interface (s_{ui}) is assumed to be equal to the surrounding soil's undrained shear strength (s_u). Furthermore, a tension cut-off condition is applied at the soil-pile interface, allowing the soil to separate from the backside of the rectangular pile. This condition is necessary for the solution procedure and has been described in previous works by Keawsawasvong and Ukritchon.[27-30] To incorporate this behavior, interface elements are introduced at the soil-pile interface using the FELA software OptumG3. These interface elements have properties identical to the surrounding clay, except that tension stresses are not permitted to occur at the interface. The surrounding clay is modeled as a homogeneous and isotropic clay exhibiting a perfectly plastic behavior, using the Tresca failure criteria. The soil unit weight (γ) and undrained shear strength (s_u) are the key factors that govern the soil profile. These parameters play a crucial role in determining the behavior and characteristics of the soil. It is important to highlight that eccentric length (e) pertains to the length of the pile's upper portion above the ground surface, which is not subjected to any constraints in terms of vertical or horizontal movement or rotation. Note that this study assumes the pile to subject to lateral load under short-term conditions and the groundwater level is located very deep and does not affect the pile. The short-term condition can be referred to the undrained conditions, which are commonly used in various geotechnical stability problems considering clayed materials.[31-37].

In this study, a dimensionless approach was employed to conduct a parametric analysis of the behavior of a three-dimensional rigid rectangular pile in cohesive soil. The analysis focused on determining the horizontal load factor. Six dimensional parameters (H, n, B, L, s_u, and γ) were considered in the study. However, to facilitate practical application, these parameters were converted into dimensionless form and expressed as a function of the normalized horizontal load factor as stated below:

$$\frac{P}{s_u BL} \propto f\left(\frac{L}{B}, \frac{H}{B}, n, \frac{e}{B}\right) \quad (1)$$

where P/s_uBL represents the normalized horizontal load factor; L/B represents the pile length-width ratio; H/B represents the pile height-width ratio; n or gL/s_u represents the overburden stress factor; e/B represents the eccentric length ratio. It should be noted that, regardless the value of s_u is large (stiff clay) or small (soft), if the value of its normalized term (n or gL/s_u) and other dimensionless parameters in Eq. (1) are the same, the result of P/s_uBL is also the same. When $n = 0$, it indicates an ideal scenario of weightless soil (*i.e.*, $\gamma = 0$). Table 1 shows the selected values of all input parameters in Eq. (1). This study provides a comprehensive analysis of the effects of various factors on the behavior of laterally loaded piles, including the parameters mentioned earlier. The investigation also examines the resulting failure patterns. The findings contribute to a better understanding of the behavior and performance of such piles under lateral loading conditions, thereby aiding in the design and optimization of pile foundations in geotechnical engineering practice.

Table 1. Selected values of all input parameters.

1	Selected values
L/B	5, 10, 20, 30, 40, 50, 60
H/B	0.5, 0.75, 1.0, 1.33, 2
e/B	0, 1, 2, 4, 8, 16
n or gL/s_u	0, 5, 10, 30, 50, 80

3. Finite element limit analysis

The numerical model of a free-head rectangular pile in cohesive soil is simulated using the finite element limit analysis software, namely OptumG3. The lower bound solution represents a conservative estimation of the exact solution of the limit load of a lateral pile, while the upper bound solution provides an upper estimation. The auto mesh adaptive method is a technique in OptumG3 that can be employed to enhance the accuracy and reliability of numerical solutions. It achieves this by adapting the mesh size in specific areas to be denser, based on the local solution behavior. Initially, an initial mesh is established, and error indicators are utilized to identify regions within the domain where the solution is inadequately represented. In the context of FELA, these areas are commonly characterized as zones with high shear dissipation, often referred to as shear dissipation control. Once these specific areas have been identified, the mesh is refined in those regions, thereby enhancing the accuracy of the solution. In this study, we employ this technique by activating this feature in OptumG3. It is important to note that, for all models, we set five adaptive iterations of mesh adaptivity. Starting with 5,000 elements and concluding with 10,000 elements after three steps of mesh adaptivity, this approach aims to reduce the disparity between the lower bound (LB) and upper bound (UB) solutions, ultimately leading to more precise and dependable results. The model of the 3D free-head rectangular pile in undrained clay with adaptive meshes is shown in Fig. 1.

In all numerical analyses conducted in this paper, the model domains are designed to be sufficiently large to fully contain any potential collapsible areas. This ensures that the failure zone does not reach or intersect the far boundaries of

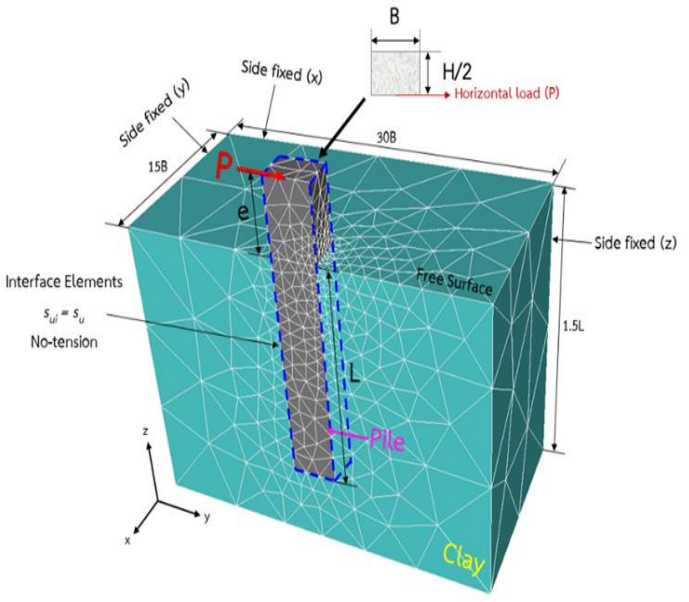

Fig. 1 Problem definition and FELA model.

the model. The model's domain has a cross-section with a width of 30B and a height of 15B. The length of the model domain is set as 1.5L. Furthermore, the boundary conditions are set according to typical practices in finite element analysis as follows. At the bottom of the domain, a zero-velocity condition is applied in all three directions (x, y, z). On the three side-planes of the model, only the velocity in the normal direction is fixed, which is equivalent to fixing all nodes on the symmetrical plane in the normal direction. The nodes are free to move in the other two tangential directions. On the top plane of the soil, a free surface condition is applied, allowing the nodes to move freely in all directions. These boundary conditions are commonly used in finite element analysis and are employed to accurately simulate the behavior of the system under investigation.

4. Verification

Figure 2 shows the comparison of numerical results for the undrained lateral capacity of free-head rectangular pile to those published papers which consists of the classical LEM solutions of the lateral capacity of the circular free-head pile proposed by Broms[7] and Georgiadis *et al.*[9] and the FEM solutions proposed by Keawsavasvong and Ukritchon.[30] Note that the result of the present study in Fig. 2 refers to the average solutions of $P/(s_uLB)$ obtained from the upper bound (UB) and lower bound (LB) calculations. The current results give the greatest value compared to those published works, where the closest studies are performed by Keawsavasvong and Ukritchon[30] and Georgiadis *et al.*[9] while the LEM solutions obtained by Broms[7] indicate significantly lower values compared to the current solutions. The average solutions obtained in the current study are consistent with the published solutions, indicating that there is good agreement between the previous works and the present findings. Specifically, all the solutions, including both the present and published ones, show a similar trend, where an increase in $P/(s_uLB)$ as L/B increases. Furthermore, the increase in $P/(s_uLB)$ is nonlinear, implying that the relationship between $P/(s_uLB)$ and L/B is not a simple linear correlation. However, the difference between the present study and those previous works are due to the differences in shape and geometry, where the solutions of this study in Fig. 2 are obtained from square piles, while those previous studies are from circular piles. Note that square or rectangular piles have a larger surface area in contact with the soil compared to circular piles of the same cross-sectional area. This increased surface area allows for more interaction and friction between the pile and the surrounding soil, providing greater resistance against lateral forces. In addition, square or rectangular piles have corners and edges that increase the perimeter of the pile's cross-section. This additional perimeter helps distribute the lateral forces more effectively along the length of the pile. In contrast, circular piles distribute the forces more evenly around the perimeter, resulting in less concentrated resistance. Overall, the current results show a similar trend to those published papers, which helps validate the accuracy of the solution. This consistency in the trend observed between the current study and the published works provides confidence in the correctness of the obtained results.

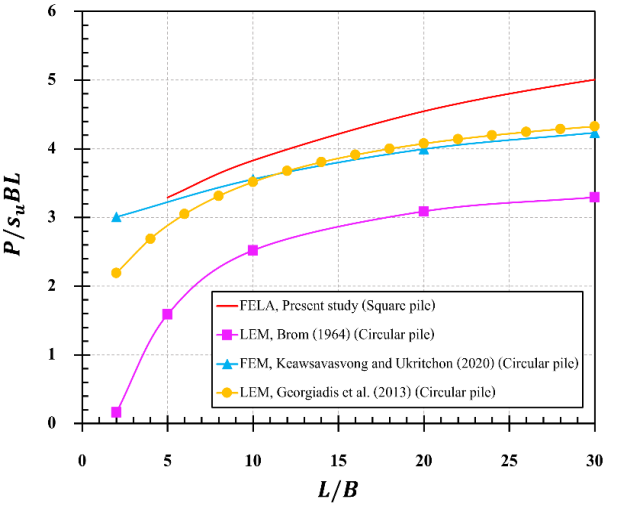

Fig. 2 Comparison of P/s_uBL solutions between the present study and previous works.

5. Results and discussion

This section focuses on the numerical results obtained from the parametric studies carried out on rigid free-head rectangular piles under lateral loading. The main aim of these

studies was to thoroughly investigate and analyze the effects of key parameters on the behavior and response of the surrounding soil. The obtained numerical results offer valuable insights into the soil's response and help to identify the crucial factors that influence the overall performance of the soil-pile system.

The influence of L/B on P/s_uBL is shown in Figs. 3(a-e), where the selected cases are H/B = 0.5 and n = 0.5, 5, 10, 30, 50, and 80, respectively. The figures comprise six separate sets of data points, each corresponding to different values of e/B, specifically 0, 1, 2, 4, 8, and 16. The results depicted in Figs. 3(a-f) demonstrate that an increase in the L/B ratio results in a nonproportional rise in the P/s_uBL value. Deep piles penetrate into deeper, more stable soil layers with higher shear strength. The increased embedment depth allows the pile to engage with stronger and more competent soil, providing greater lateral resistance against applied loads. In addition, longer piles have a larger surface area in contact with the surrounding soil. This increased contact area promotes a higher level of soil-pile interaction, resulting in a more significant transfer of lateral loads from the pile to the soil. The increased interaction improves the overall lateral capacity of the pile. Figs. 4 to 7 exhibit a sequence of plots that maintain consistent parameter settings as depicted in Fig. 3, with the exception of the H/B value. In these figures, the H/B ratio is varied across different scenarios, specifically with values of H/B = 0.75, 1.00, 1.33, and 2.00. According to the data in Figs. 3-7, the parameter n plays a crucial role in the lateral load capacity of piles, in which an increase in the overburden ratio n leads to a higher value of P/s_uBL due to the surrounding soil becoming more

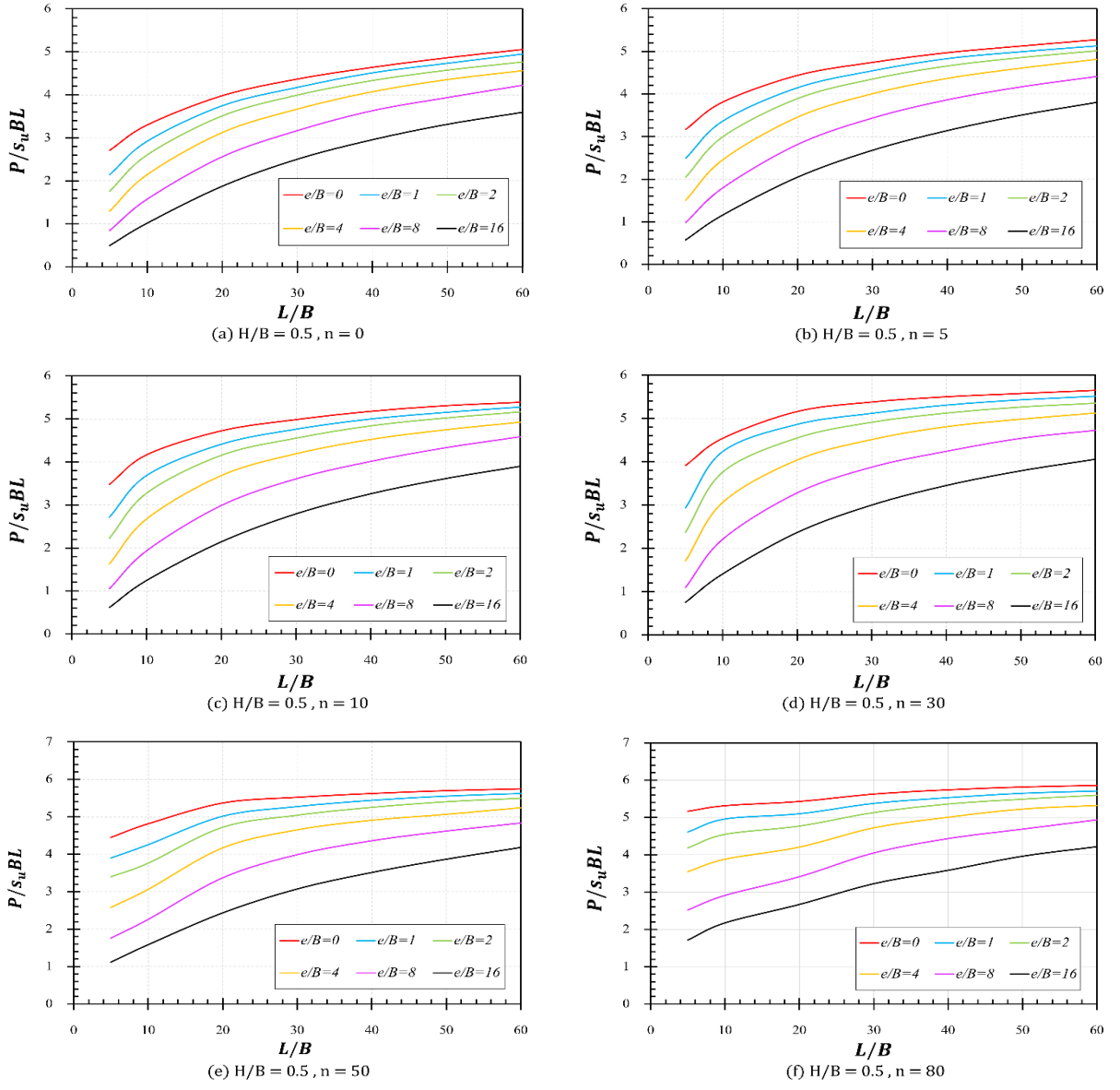

Fig. 3 Influence of L/B on P/s_uBL for rectangular piles, where H/B = 0.5: (a) n = 0; (b) n = 5; (c) n = 10; (d) n = 30; (e) n = 50; (f) n = 80.

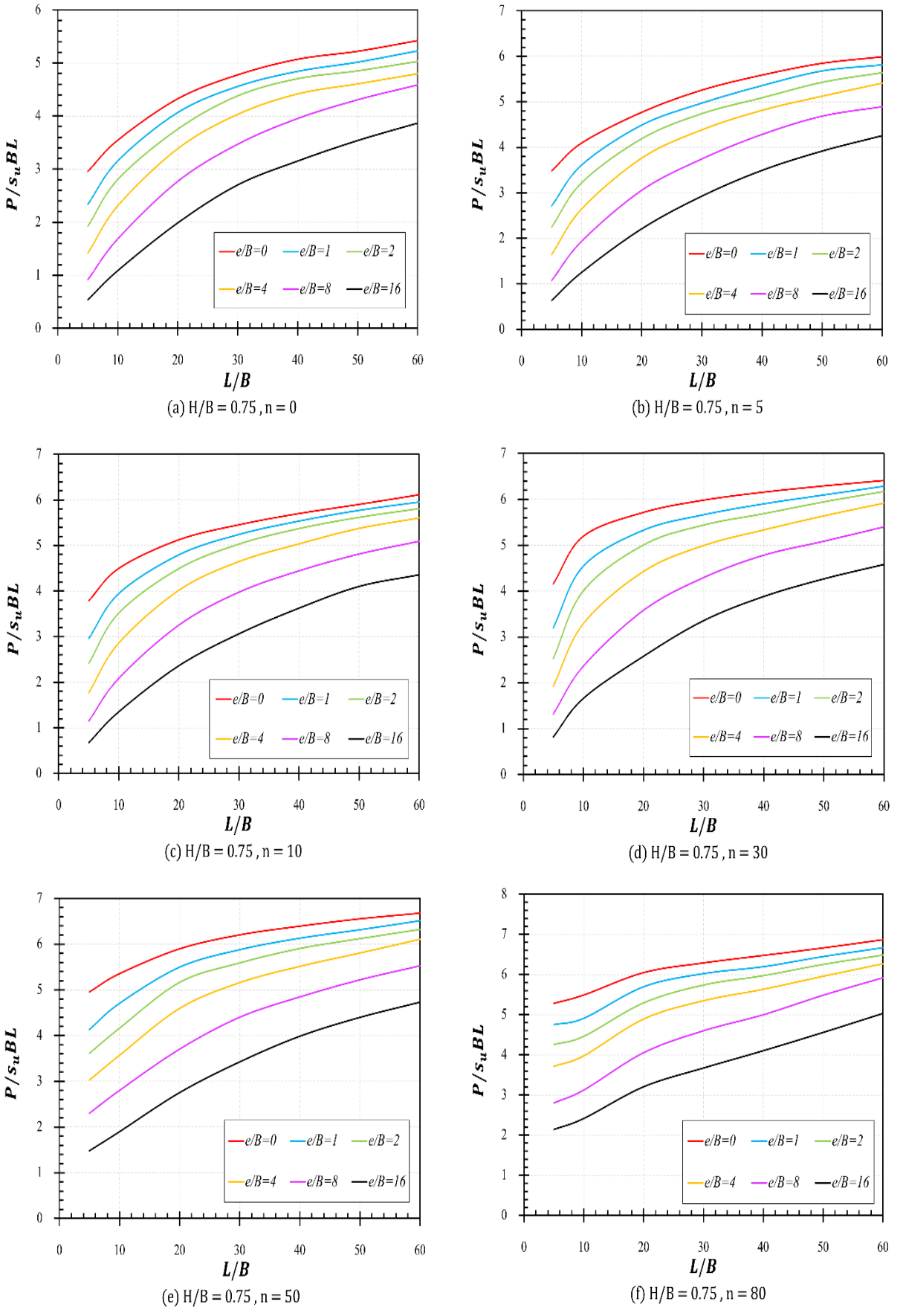

Fig. 4 Influence of L/B on P/s_uBL for rectangular piles, where H/B = 0.75: (a) n = 0; (b) n = 5; (c) n = 10; (d) n = 30; (e) n = 50; (f) n = 80.

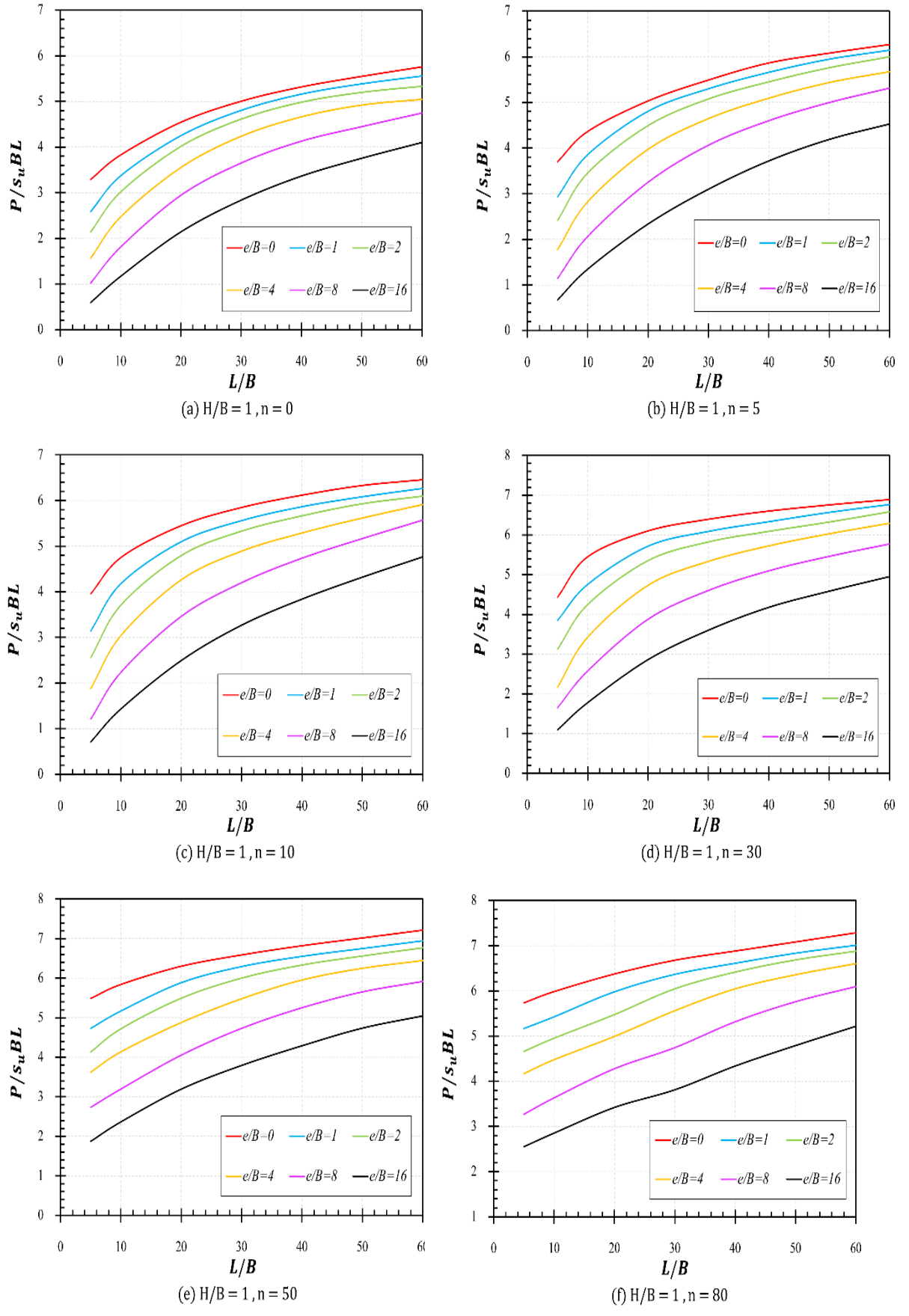

Fig. 5 Influence of L/B on P/s_uBL for rectangular piles, where H/B = 1.0: (a) n = 0; (b) n = 5; (c) n = 10; (d) n = 30; (e) n = 50; (f) n = 80.

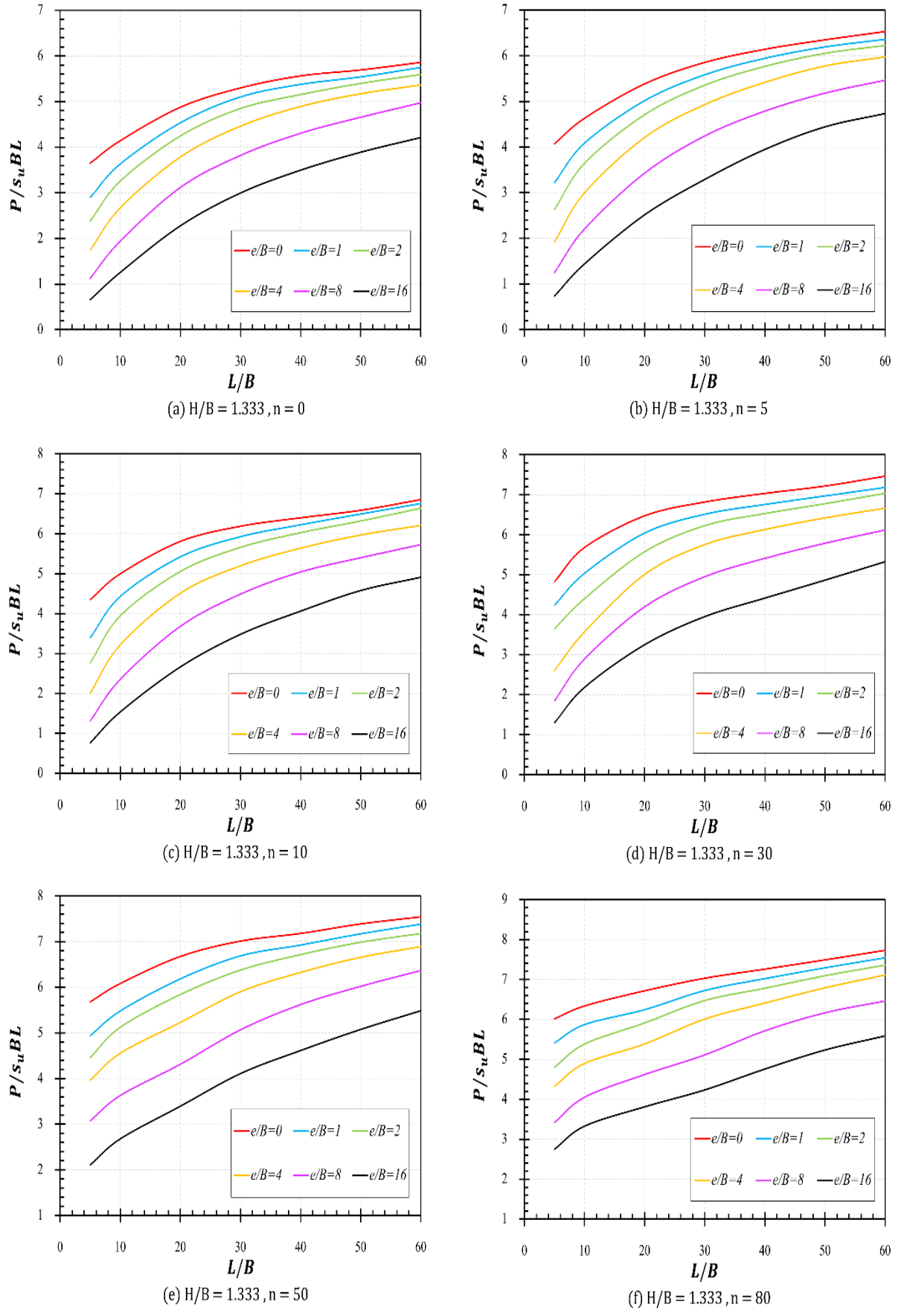

Fig. 6 Influence of *L/B* on P/s_uBL for rectangular piles, where *H/B* = 1.33: (a) *n* = 0; (b) *n* = 5; (c) *n* = 10; (d) *n* = 30; (e) *n* = 50; (f) *n* = 80.

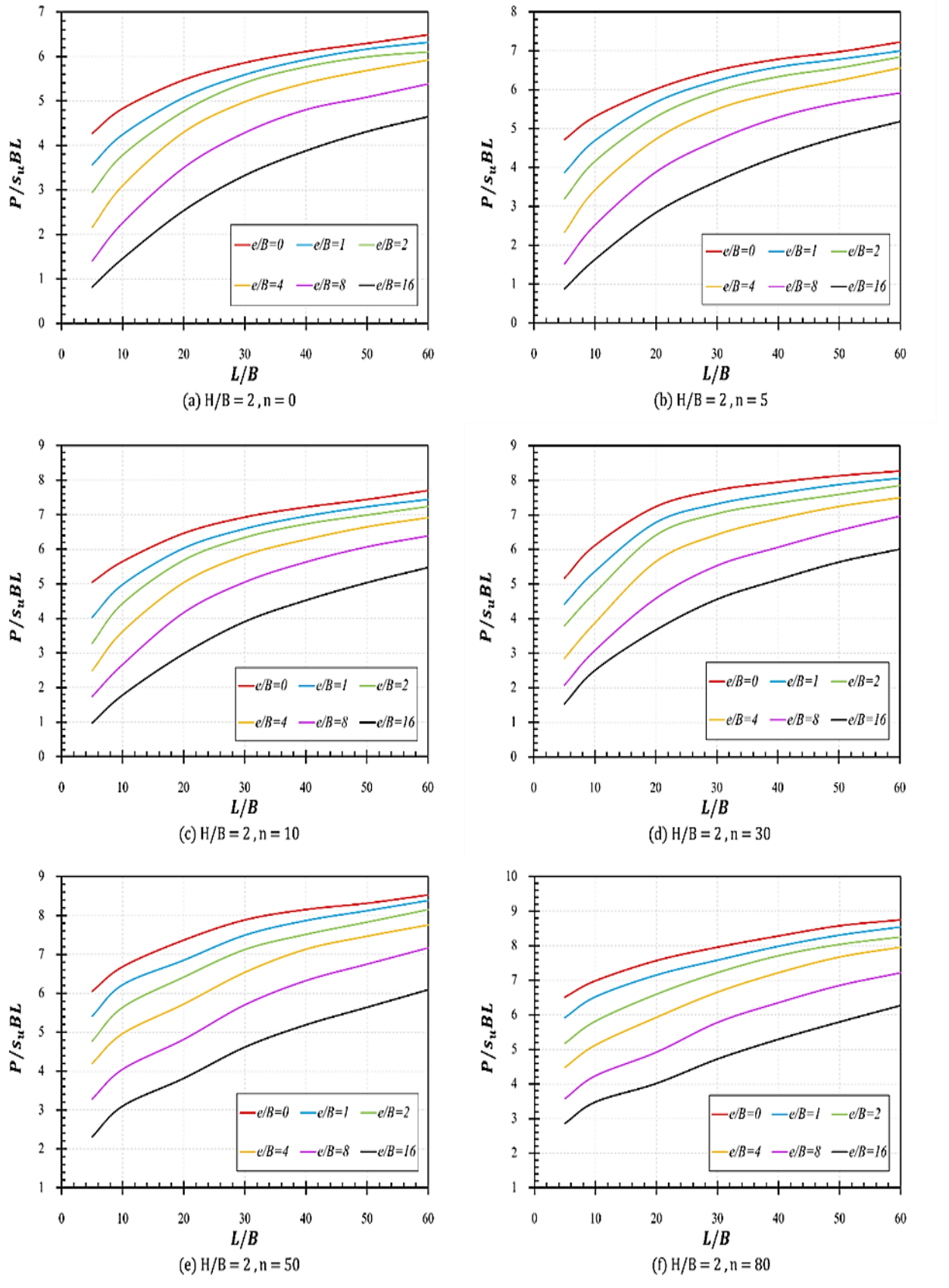

Fig. 7 Influence of L/B on P/s_uBL for rectangular piles, where H/B = 2.0: (a) n = 0; (b) n = 5; (c) n = 10; (d) n = 30; (e) n = 50; (f) n = 80.

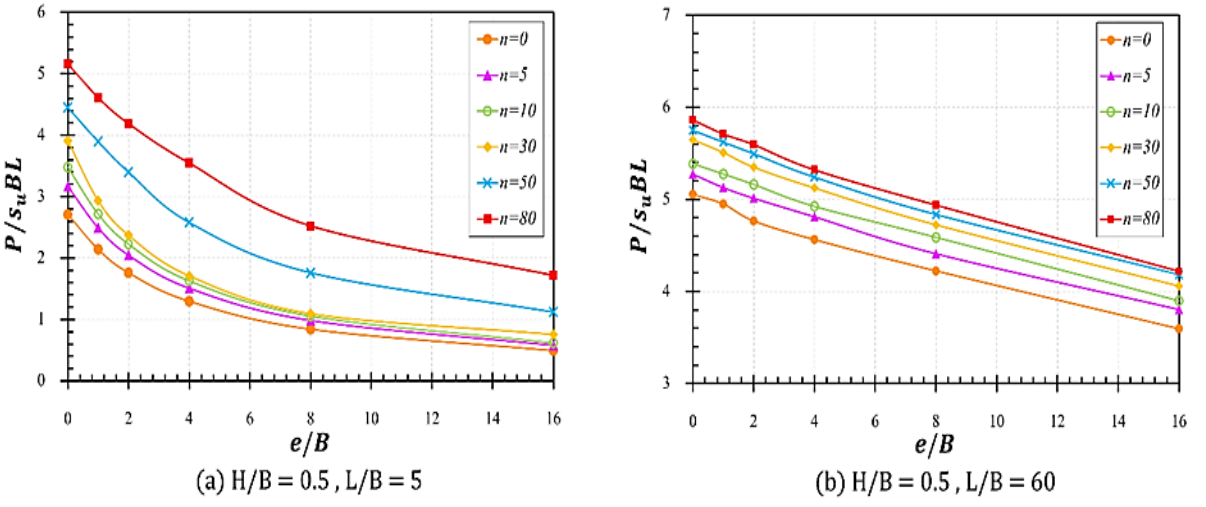

Fig. 8 Influence of e/B on P/s_uBL for rectangular piles, where H/B = 0.5: (a) L/B = 5; (b) L/B = 60.

compacted and denser. As pointed out by Keawsavasvong and Ukritchon,[30] a higher unit weight signifies a greater mass of soil within a given volume. This increased soil mass contributes to a higher overall lateral resistance against applied loads. The greater weight of the soil provides additional passive resistance to the lateral movement of the pile, enhancing the lateral capacity.

Figure 8 shows the influence of e/B on P/s_uBL, where the selected samples are in the case of H/B = 0.5 and L/B = 5 and 60. A non-linear decreasing relationship between e/B and P/s_uBL can be seen in Fig. 8a. As e/B increases, it can result in a reduction in the lateral load capacity of the soil. The lateral capacity of a pile primarily depends on the resistance offered by the surrounding soil. When the pile is subjected to an eccentric load, the effective soil resistance on one side of the pile decreases due to the reduced soil-pile interaction. This reduced resistance contributes to a decrease in the lateral capacity of the pile, which is similar to the finding by Chaonoi *et al*..[38] In Fig. 8b, the relationship pattern between e/B and P/s_uBL is shifted due to piles becoming slenderer (L/B = 60), and the distribution of lateral loads along the pile length becomes more uniform. This can lead to a more predictable and linear response in terms of the lateral load capacity of the soil.

Figure 9 shows the influence of H/B on P/s_uBL where L/B = 5 and e/B = 0. The figures comprise six separate sets of data points, each corresponding to different values of n specifically 0, 5, 10, 30, 50, and 80. The relationship between H/B and P/s_uBL is non-linear for all cases. It is clearly observed that a variation of H/B significantly affects the value of P/s_uBL, as the H/B ratio increases, the lateral load capacity of the soil tends to increase as well. The lateral load capacity of the soil is affected by the ratio of pile height to pile base width (H/B ratio), and the specific effects vary depending on the dimensions of the pile. When the H/B ratio is small, as observed in short and wide piles, the lateral load capacity of the soil tends to decrease. This decrease can be attributed to the wider base of the pile, which spreads the load over a larger soil area, consequently reducing the soil's resistance to lateral loads. In contrast, when the H/B ratio is increased, indicating a taller and narrower pile configuration, the soil's lateral load capacity improves. According to Keawsawasvong *et al*,[26] this improvement is due to several factors. Firstly, the increased pile height facilitates a more significant mobilization of soil resistance against lateral loads. Secondly, the taller pile configuration provides enhanced soil confinement, thereby boosting the soil's ability to withstand lateral loads.

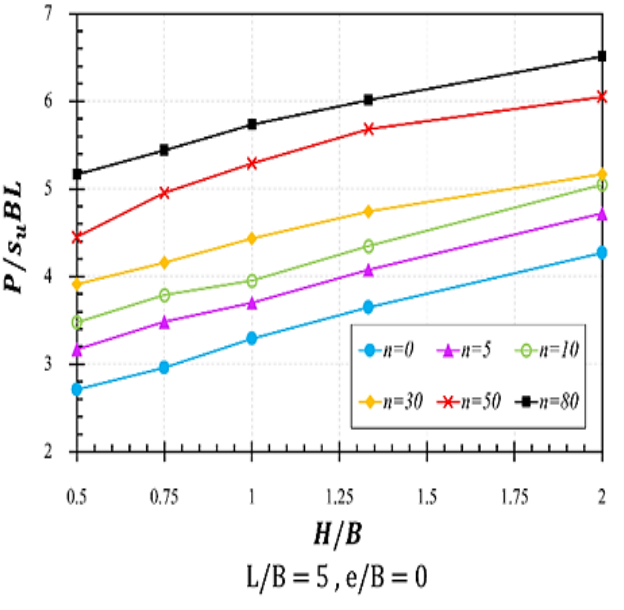

Fig. 9 Influence of H/B on P/s_uBL for rectangular piles, where n = 0.5 and e/B = 5.

The impact of variation in the *H/B* ratio on failure mechanisms is illustrated in Fig. 10. The specific cases considered are *e/B* = 0, *n* = 10, *L/B* = 40, and different *H/B* values: 0.5, 0.75, 1, 1.33, and 2. From Fig. 10(a), it is evident that when *H/B* is small, the shear dissipation predominantly occurs in the upper half of the soil. This is due to a decrease in shear resistance along the pile-soil interface caused by the pile's cross-section. Interestingly, these upper layers exhibit greater susceptibility to shear deformation, resulting in significant shear energy dissipation. As the *H/B* ratio increases, indicating a taller and narrower pile, the failure mechanisms of the soil shift towards a combination of sliding and rotational failure. This change in failure behavior can be attributed to the enhanced confinement of the soil around the pile, which promotes rotational failure. In this mode of failure, the soil undergoes substantial deformation and rotation around the pile due to the heightened lateral load demands imposed on the system, as depicted in Figs. 10(b-e). The influence of *e/B* variation on failure mechanisms is demonstrated in Fig. 11. The selected examples involve *H/B* = 1.33, *n* = 10, *L/B* = 40, and varying *e/B* values: 0, 1, 2, 4, 8, and 16. Figure 11(a) depicts a fixed head pile (*e/B* = 0), clearly illustrating the presence of the passive failure zone. As *e/B* increases, the sensitive zone shifts closer to the pile interface due to non-uniform lateral load distribution. However, the passive failure zone remains noticeable, as observed in Figs. 11(b-e).

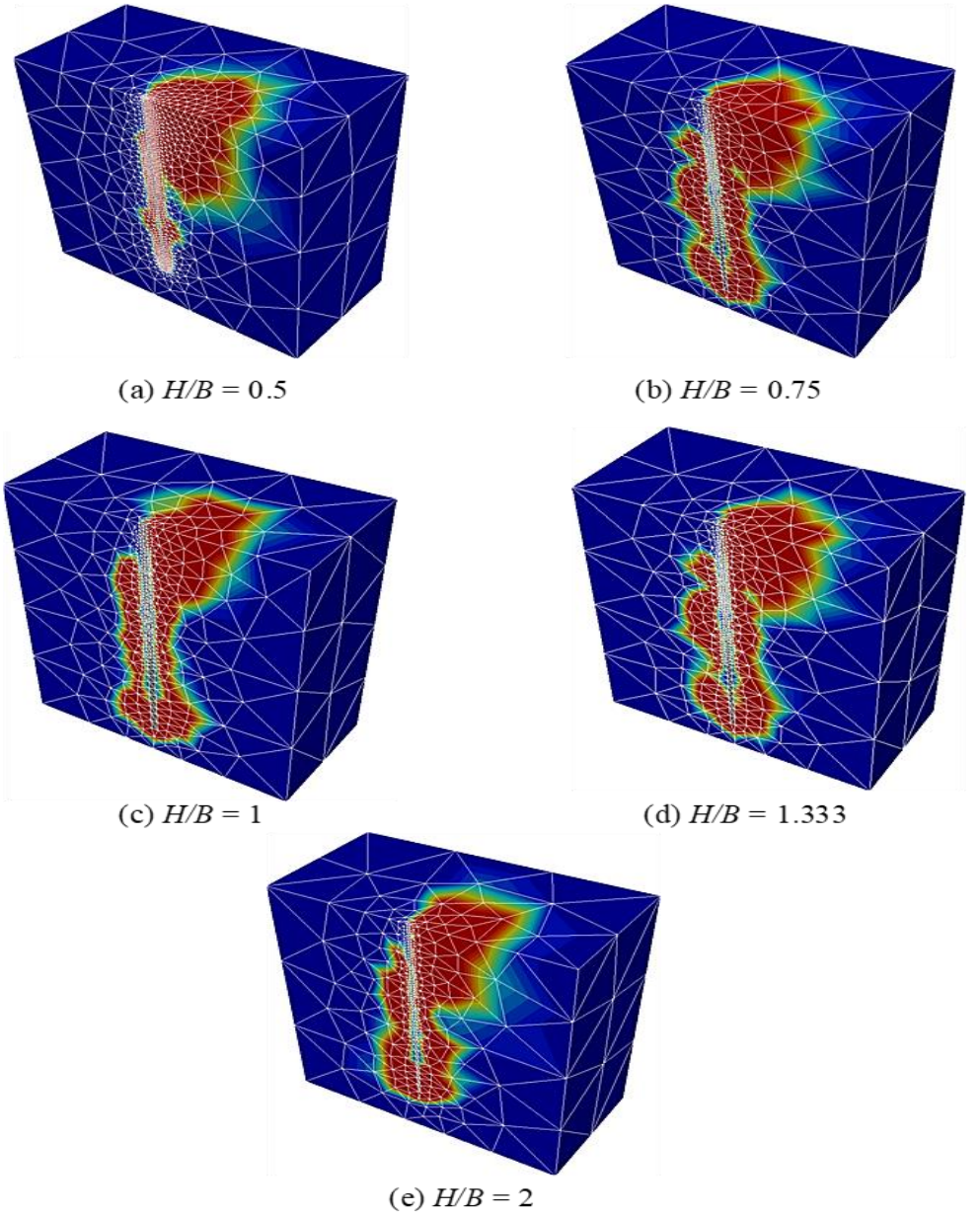

(a) *H/B* = 0.5 (b) *H/B* = 0.75

(c) *H/B* = 1 (d) *H/B* = 1.333

(e) *H/B* = 2

Fig. 10 Effect of *H/B* on failure mechanisms (*e/B* = 0, *n* = 10, *L/B* = 40): (a) *H/B* = 0.5; (b) *H/B* = 0.75; (c) *H/B* = 1; (d) *H/B* = 1.333; (e) *H/B* = 2.

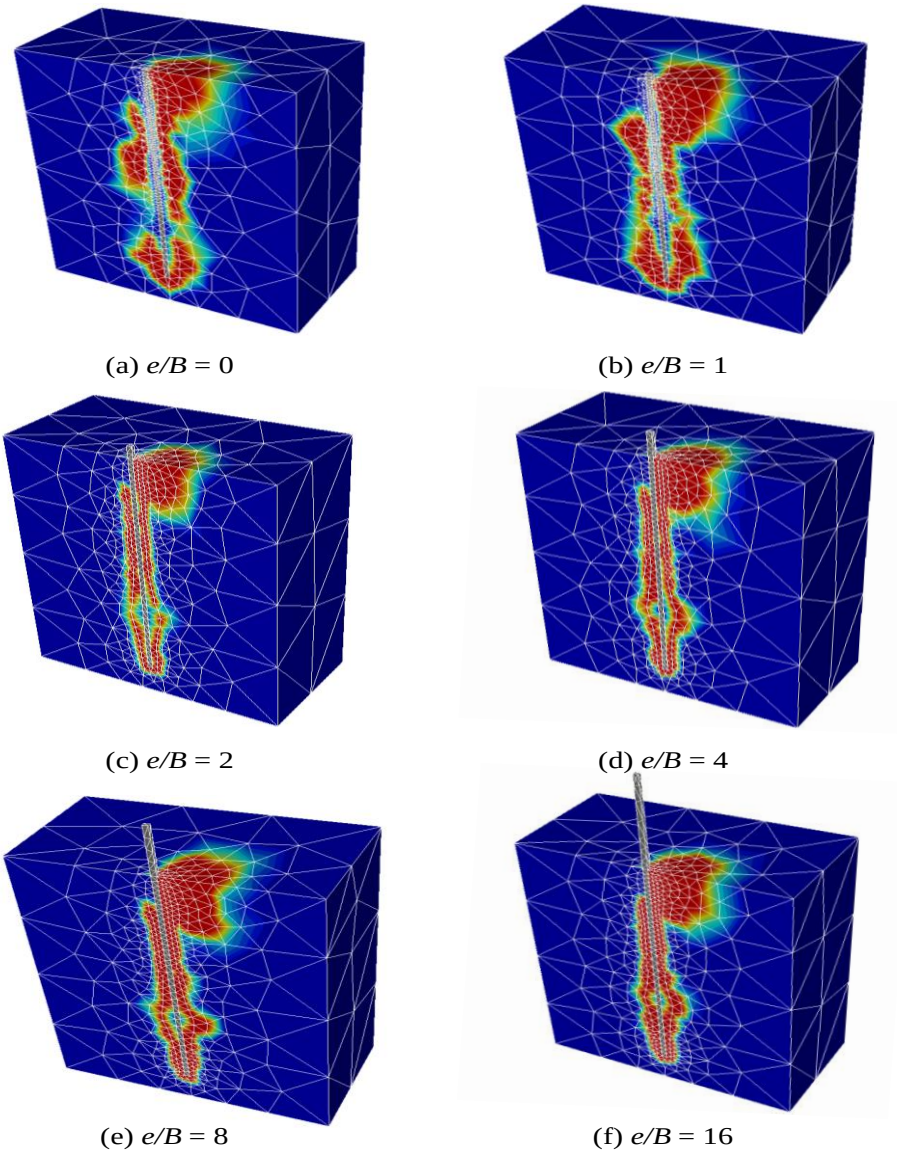

Fig. 11 Effect of *e/B* on failure mechanisms (*H/B* = 1.333, *n* = 10, *L/B* = 40): (a) *e/B* = 0; (b) *e/B* = 1; (c) *e/B* = 2; (d) *e/B* = 4; (e) *e/B* = 8; (f) *e/B* = 16.

6. Artificial neural networks (ANN)

Belonging to the supervised learning category, the artificial neural network (ANN) is a machine learning algorithm that replicates the functions of the human brain or the biological nervous system. It forms a network resembling the structure of the human brain, facilitating human-like learning through numerous interconnected neurons. These interconnected neurons with weighted connections exhibit intricate and nonlinear behavior. Typically, ANN models comprise three layers: input, hidden, and output layers, as depicted in Fig. 12. Learning and training processes involve various aspects of ANN models, including the number of hidden layers, weight connections, and bias or constant value.

The multilayer perceptron (MLP) is a type of artificial neural network (ANN) that is commonly used in machine learning. It is a feed-forward neural network, meaning that information flows in one direction, from the input layer through the hidden layers to the output layer, without any cycles or loops. Composed of nodes, also known as neurons, the MLP is organized into distinct layers. Typically, it consists of an input layer, one or more hidden layers, and an output layer. The nodes within the hidden layers employ nonlinear activation functions, such as the sigmoid or hyperbolic tangent function, introducing nonlinearity to the network's computations. Throughout the training phase, the MLP employs the backpropagation algorithm to adjust the weights connecting the nodes. This algorithm assesses the discrepancy between the network's predicted output and the desired output and subsequently propagates this error backward through the network, facilitating the necessary weight updates. By

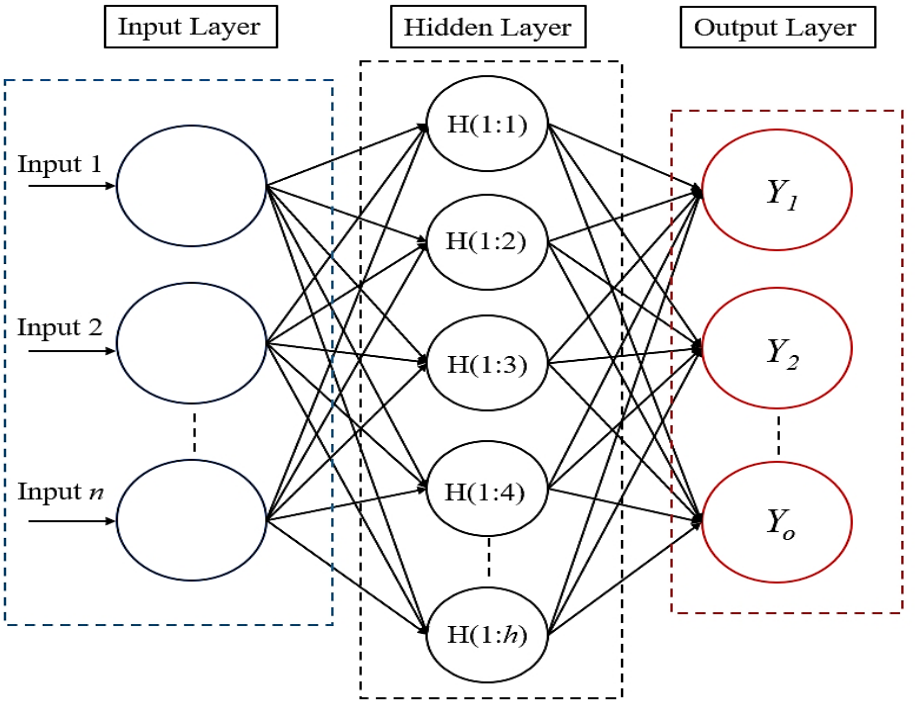

Fig. 12 Configuration of an ANN model.

iteratively refining the weights based on the computed errors, the MLP aims to minimize the overall disparity between its predictions and the intended outcomes. This process enhances the network's ability to accurately capture complex relationships within the data. The MLP's flexibility and capacity to model intricate patterns and relationships have established its significance in various machine learning tasks, including classification, regression, and pattern recognition. Its utilization of backpropagation for weight adjustment enables effective learning from data and the ability to make predictions on unseen instances. The expression that defines the output of an MLP network is as follows:

$$y_o = f(\sum_{i=1}^{h} w_{ho}\, x_h + bias) \quad (2)$$

where y_o denotes the output; x_h denotes activation of hth hidden layer node; w_{ho} denotes the weight connection between hth hidden layer node and oth output layer node; $f(\,)$ denotes the activation function; and h denotes the number of hidden neurons.

In order to evaluate the performance of the prediction model and mitigate the risk of overfitting, the input dataset is partitioned into two parts: the training dataset and the testing dataset. This conventional division enables the assessment of the MLP's accuracy when presented with novel or unseen data. For this study, the dataset comprises a total of 1260 samples. The partitioning process assigns 70% of the samples, equivalent to 890 samples, to the training dataset, while the remaining 30%, corresponding to 370 samples, are allocated to the testing dataset. This allocation scheme is visually depicted in Table 2. The input and output data from the dataset undergo a standardization process before analysis using an artificial neural network model to prevent potential learning errors that may arise from the disparate impact of different data ranges. The input data is standardized, while the output prediction is kept in a standardized format. Consequently, a reverse calculation is required to convert the standardized data back to its original format in order to obtain the actual prediction results. By employing the standardized equations, calculations can be performed:

$$z = \frac{x-\mu_x}{\sigma_x} \quad (3)$$

where $z(x)$ is a standardized value, m is the average of value, s is the standard deviation, and x is the value.

Table 2. Case processing summary from SPSS.

		N	Percent
Sample	Training	890	70.0%
	Testing	370	30.0%
Valid		1260	100.0%
Excluded		0	
Total		1260	

By utilizing the SPSS software, the optimal number of neurons in the hidden layer is automatically determined to construct the MLP model with the utmost accuracy. The range of 1-50 neurons is considered, and based on Fig. 13, it is evident that the MLP model achieves its highest prediction

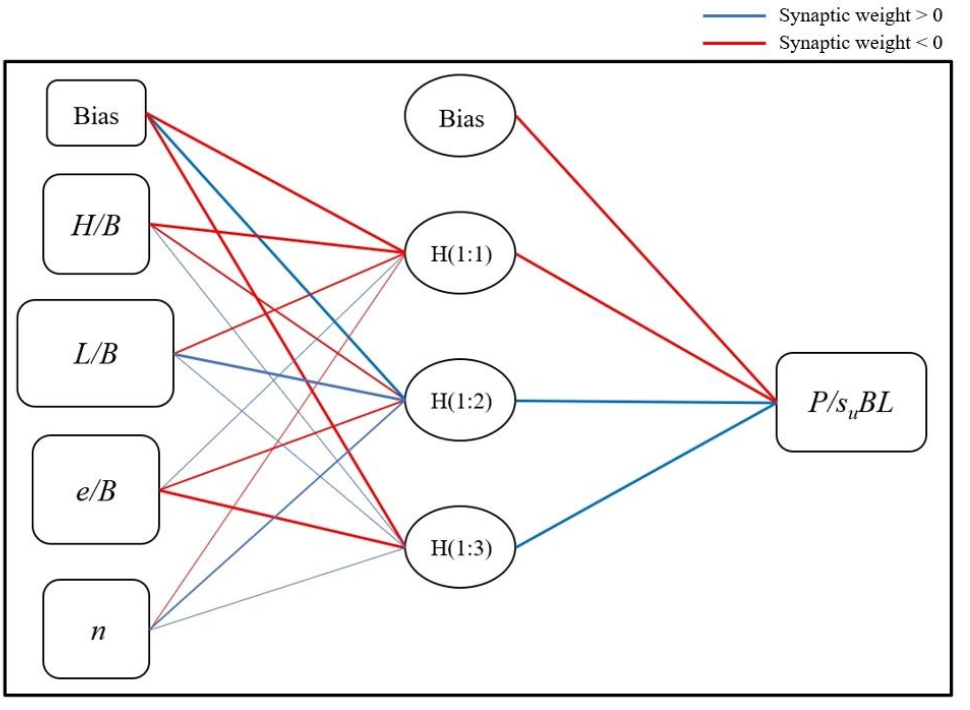

Fig. 13 Neural network for the four dependent variables and one covariance.

accuracy when the hidden layer consists of 3 neurons. Table 3 provides a concise summary of the network architecture and model structure. The input layer of the MLP incorporates four covariates, namely *H/B*, *L/B*, *e/B*, and *n*. The activation function chosen for the hidden layer is the hyperbolic tangent function. Furthermore, the output layer of the MLP model encompasses the P/s_uBL dependent variable. For model evaluation, the sum of squares serves as the error function.

The performance of the MLP model is evaluated through statistical equations, including the coefficient of determination (R^2), mean absolute error (*MAE*), root mean square error (*RMSE*), and variance accounted for (*VAF*). These equations are utilized to compare the results obtained from the FELA method with those obtained from the MLP method. The calculations can be conducted using the following equations:

$$R^2 = 1 - \frac{SSE}{SST} = 1 - \frac{\sum_{i=1}^{n}(y_i - x_i)^2}{\sum_{i=1}^{n}(y_i - \bar{y})^2} \quad (4)$$

$$MAE = \frac{1}{n} \times \sum_{i=1}^{n} |y_i - x_i| \quad (5)$$

$$RMSE = \sqrt{\frac{1}{n} \times \sum_{i=1}^{n}(y_i - x_i)^2} \quad (6)$$

$$VAF = \left(1 - \frac{var(y_i - x_i)}{var(y_i)}\right) \times 100\% \quad (7)$$

where *SSE* is the sum of square errors, *SST* is the total sum of squares, y_i is the FELA value, x_i is the MLP value, $\bar{y}$ is the average of the FELA values, and *n* is the number of datasets. Under the best conditions, R^2 is equal to one, *RMSE* and *MAE* are zero, and *VAF* is 100%. These equations enable the assessment and comparison of the accuracy of the prediction model based on the MLP method against the results obtained from utilizing the FELA method.

Table 3. Network information for the structure of the MLP model.

Input layer	Covariates	1	*H/B*
		2	*L/B*
		3	*e/B*
		4	*n*
	Number of Units		4
	Rescaling Method for Covariates		Standardized
Hidden Layer(s)	Number of Hidden Layers		1
	Number of Units in Hidden Layer		3
	Activation Function		Hyperbolic tangent
Output Layer	Dependent Variables	1	P/s_uBL
	Number of Units		1
	Rescaling Method for Scale Dependents		Standardized
	Activation Function		Identity
	Error Function		Sum of Squares

Table 4 provides a comprehensive overview of the learning outcomes pertaining to the training process and the performance assessment of the MLP model when confronted with novel data during the testing phase. The sum of squares

serves as the error function to ascertain the model's error. The model's operation is halted upon the cessation of any further changes in the sum of squares. This criterion is meticulously regulated throughout the testing process. According to the findings, the sum of squares values for the training and testing processes are recorded as 15.670 and 7.821, respectively. The iterative adaptation of weights throughout the training and testing process culminates in the most precise result, whereby the sum of squares no longer diminishes upon the modification of outcomes. The weights associated with each layer are outlined in Table 5, showcasing their respective values employed in the prediction of the normalized horizontal load factor via an MLP model comprising 3 hidden neurons and utilizing the hyperbolic tangent function as the activation function.

Upon comparing the predictive performance of the weights obtained through the MLP model derived from a dataset consisting of 1260 samples, the accuracy was evaluated using four statistical equations: R^2, *MAE*, *RMSE*, and *VAF* (%). Fig. 14 presents a visual representation of the comparative analysis conducted between the true values obtained from the FELA method and those predicted by the MLP model. The results indicate that the R^2, *MAE*, *RMSE*, and *VAF* (%) values are recorded as 0.962, 0.252, 0.317, and 96.24%, respectively.

Table 4. A model summary of training and testing data.

Training	Sum of Squares Error	15.670
	Relative Error	0.035
	Stopping Rule Used	1 consecutive step(s) with no decrease in error
Testing	Sum of Squares Error	7.821
	Relative Error	0.045

Table 5. Weight values of parameter estimates.

		Predicted			
		Hidden Layer			Output Layer
Predictor		H (1:1)	H (1:2)	H (1:3)	P/s_uBL
Input layer	(Bias)	-0.387	1.350	-0.617	
	H/B	-0.470	-0.231	0.171	
	L/B	-0.222	0.934	0.033	
	e/B	0.078	-0.197	-0.651	
	n	-0.028	0.260	0.202	
Hidden Layer	(Bias)				-0.755
	H (1:1)				-0.997
	H (1:2)				1.360
	H (1:3)				1.103

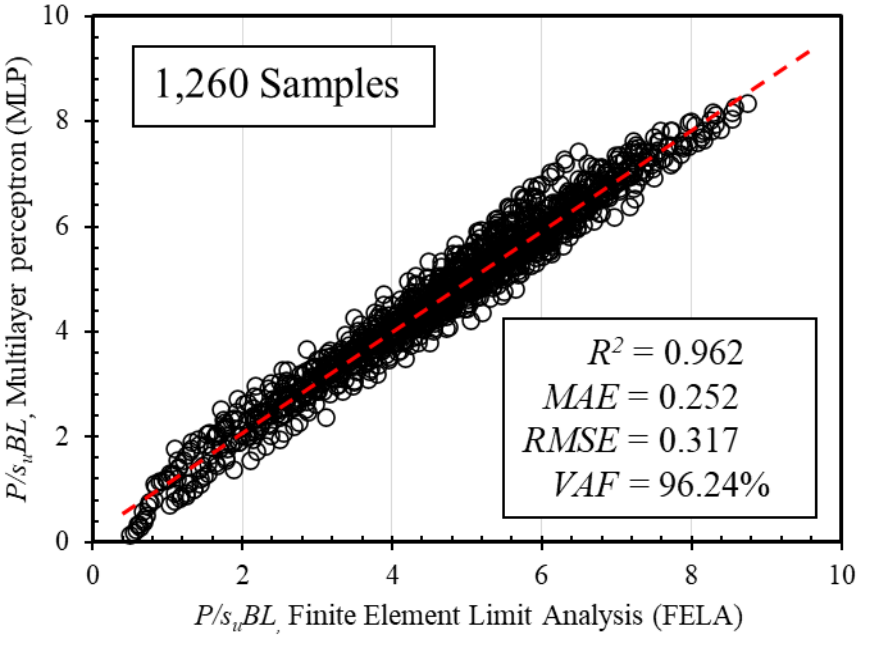

Fig. 14 Performance of FELA method and MLP model to predict the normalized horizontal load factor (P/s_uBL).

These outcomes suggest that the R^2 value approaches 1, while the *MAE* and *RMSE* values exhibit close proximity to zero, and the *VAF* (%) value approaches 100%. Consequently, the utilization of the MLP model demonstrates a commendable level of accuracy in forecasting the normalized horizontal load factor for problems associated with rectangular or square free-head piles, considering the dimensionless factors *H/B*, *L/B*, *e/B*, and *n*.

Through the investigation of the interrelationships between input data comprising four covariates (*H/B*, *L/B*, *e/B*, and *n*) and a dependent variable, specifically the normalized horizontal load factor (P/s_uBL), one can ascertain the importance of different parameters in influencing the value of E. This analysis enables the identification of parameters that wield the most substantial influence on P/s_uBL through sensitivity analysis. As depicted in Fig. 15, it becomes apparent that alterations in the value of *L/B* yield the most pronounced fluctuations in P/s_uBL. Subsequently, the parameters *e/B*, *H/B*, and *n* exhibit diminishing levels of impact on P/s_uBL in descending order.

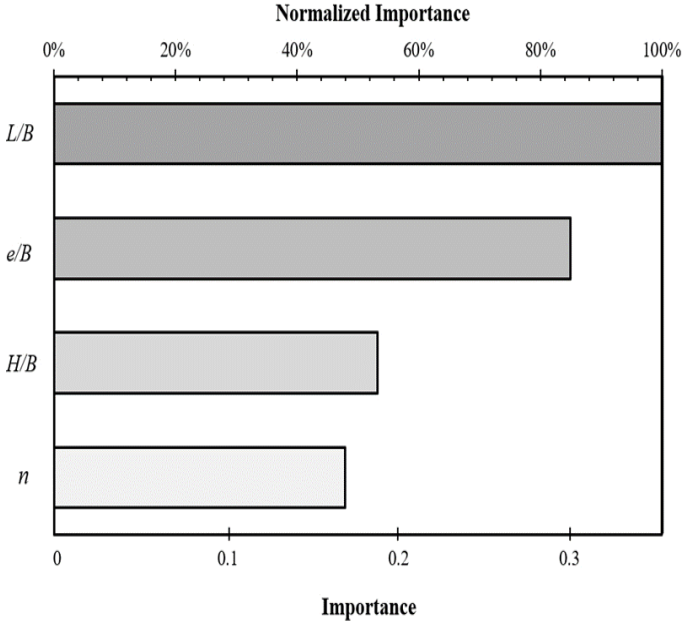

Fig. 15 Importance and Normalized Importance of the input parameters on the prediction.

7. Conclusion

This paper presents the limit state solutions for undrained lateral capacity of free-head rectangular/square piles in cohesive soils using the FELA framework. Parametric studies are conducted on three-dimensional rigid piles subjected to lateral loads, providing valuable insights into the behavior and failure mechanisms of the surrounding soil. The results highlight the influence of various factors, including pile length-width ratio (*L/B*), height-width ratio (*H/B*) of the pile, eccentricity (*e/B*) of the lateral load, and overburden stress (*n*), on soil performance. Based on the study, the following conclusions are drawn.

1) The numerical findings reveal the critical role of the pile length-width ratio in the normalized horizontal load factor. Increasing this ratio enhances the lateral load capacity. Similarly, an increase in the height-width ratio improves the soil's lateral load capacity, while greater eccentricity leads to a more concentrated load distribution and higher shear stresses. The overburden stress contributes to improved soil interlocking and lateral load resistance.

2) The failure mechanisms of lateral piles are influenced by the pile's height-width ratio and the eccentricity of the lateral load. As the pile's height-width ratio increases, there is a transition from predominantly sliding failure to a combination of sliding and rotational failure. Increasing eccentricity results in a higher concentration of forces, increasing the likelihood of rotational failure around the pile interface while still maintaining a passive failure zone at the ground surface. These insights contribute to enhanced pile foundation design and analysis in geotechnical engineering.

3) To predict the normalized horizontal load factor, an MLP model based on Artificial Neural Networks (ANN) is employed. The analysis considers four independent variables: *H/B*, *L/B*, *e/B*, and *n*. The model's performance is evaluated using statistical equations such as R^2, *MAE*, *RMSE*, and *VAF* (%). The evaluation results demonstrate a high level of precision, with R^2 approaching 1, *MAE* approaching 0, *RMSE* approaching 0, and *VAF* (%) reaching 100%. This analysis underscores the effectiveness of using the MLP model with three neurons and the hyperbolic tangent function as the activation function for predicting the normalized horizontal load factor. Among the independent variables, *L/B* has the most significant impact on the normalized horizontal load factor, followed by *e/B*, *H/B*, and *n* in descending order.

4) It is important to note that this study is limited to numerical investigations using FELA. For future research, experimental results should be conducted and compared with the numerical findings presented in this study.

Acknowledgement

This work was supported by the Thailand Science Research and Innovation Fundamental Fund fiscal year 2023. The first author would like to thank Faculty of Engineering, Thammasat School of Engineering, Thammasat University, for the graduate scholarship. This research was funded by National Science, Research and Innovation Fund (NSRF), and King Mongkut's University of Technology North Bangkok with Contract no. KMUTNB–FF–66–12.

Conflict of Interest

There is no conflict of interest.

Supporting Information

Not applicable.

References

[1] P. Kannaujiya, S. Jaiswal, V. B. Chauhan, Studies on the piled raft foundation for a high-rise building using finite element modeling, *Lecture Notes in Civil Engineering. Singapore: Springer Singapore*, 2021: 245-252, doi: 10.1007/978-981-16-1993-9_26.

[2] S. Alzabeebee, J. T. Chavda, S. Keawsawasvong, Analysis of bored pile subjected to machine vibration: an insight into the influence of the soil-pile interface coefficient, *Transportation Infrastructure Geotechnology*, 2022, 1-17, doi: 10.1007/s40515-022-00247-1.

[3] V. Q. Lai, S. Keawsawasvong, J. Shiau, Analysis of shaft-grouted piles using load-transfer method, *International Journal of Geosynthetics and Ground Engineering*, 2022, **8**, 1-10, doi: 10.1007/s40891-022-00351-9.

[4] B. Ukritchon, S. Keawsawasvong, Design equations of uplift capacity of circular piles in sands, *Applied Ocean Research*, 2019, **90**, 101844, doi: 10.1016/j.apor.2019.06.001.

[5] B. Ukritchon, S. Keawsawasvong, Undrained lower bound solutions for end bearing capacity of shallow circular piles in non-homogeneous and anisotropic clays, *International Journal for Numerical and Analytical Methods in Geomechanics*, 2020, **44**, 596-632, doi: 10.1002/nag.3018.

[6] B. Ukritchon, J. C. Faustino, S. Keawsawasvong, Numerical investigations of pile load distribution in pile group foundation subjected to vertical load and large moment, *Geomechanics and Engineering*, 2016, **10**, 577-598, doi: 10.12989/gae.2016.10.5.577.

[7] B. B. Broms, Lateral resistance of piles in cohesive soils, *Journal of the Soil Mechanics and Foundations Division*, 1964, **90**, 27-63, doi: 10.1061/jsfeaq.0000611.

[8] G. G. Meyerhof, S. K. Mathur, A. J. Valsangkar, Lateral resistance and deflection of rigid walls and piles in layered soils, *Canadian Geotechnical Journal*, 1981, **18**, 159-170, doi: 10.1139/t81-021.

[9] K. Georgiadis, M. Georgiadis, C. Anagnostopoulos, Lateral bearing capacity of rigid piles near clay slopes, *Soils and Foundations*, 2013, **53**, 144-154, doi: 10.1016/j.sandf.2012.12.010.

[10] I. Al-abboodi, T. T. Sabbagh, Numerical modelling of passively loaded pile groups, Geotechnical and Geological Engineering, 2019, **37**, 2747-2761, doi: 10.1007/s10706-018-00791-z.

[11] E. Conte, L. Pugliese, A. Troncone, M. Vena, A simple approach for evaluating the bearing capacity of piles subjected to inclined loads, *International Journal of Geomechanics*, 2021, **21**, doi: 10.1061/(asce)gm.1943-5622.0002215.

[12] K. Georgiadis, Variation of limiting lateral soil pressure with depth for pile rows in clay, *Computers and Geotechnics*, 2014, **62**, 164-174, doi: 10.1016/j.compgeo.2014.07.011.

[13] K. Georgiadis, M. Georgiadis, Undrained lateral pile response in sloping ground, *Journal of Geotechnical and Geoenvironmental Engineering*, 2010, **136**, 1489-1500, doi: 10.1061/(asce)gt.1943-5606.0000373.

[14] S. Keawsawasvong, Limit state solutions of laterally loaded pile in cohesive soils by finite element analysis, M. Eng. Dissertation, Chulalongkorn University, 2014.

[15] S. Keawsawasvong, B. Ukritchon, Failure modes of laterally loaded piles under combined horizontal load and moment considering overburden stress factors, *Geotechnical and Geological Engineering*, 2020, **38**, 4253-4267, doi: 10.1007/s10706-020-01293-7.

[16] Y. Zhang, K. H. Andersen, G. Tedesco, Ultimate bearing capacity of laterally loaded piles in clay - Some practical considerations, *Marine Structures*, 2016, **50**, 260-275, doi: 10.1016/j.marstruc.2016.09.002.

[17] J. Yu, M. Huang, C. Zhang, Three-dimensional upper-bound analysis for ultimate bearing capacity of laterally loaded rigid pile in undrained clay, *Canadian Geotechnical Journal*, 2015, **52**, 1775-1790, doi: 10.1139/cgj-2014-0390.

[18] J. Yu, M. Huang, C. Zhang, Ultimate lateral resistance of laterally loaded piles in undrained clay. Frontiers in Offshore Geotechnics III, CRC Press, 2015: 661-666, doi: 10.1201/b18442-88.

[19] A. Klar, M. F. Randolph, Upper-bound and load-displacement solutions for laterally loaded piles in clays based on energy minimisation, *Géotechnique*, 2008, **58**, 815-820, doi: 10.1680/geot.2007.00197.

[20] J. D. Murff, J. M. Hamilton, P-ultimate for undrained analysis of laterally loaded piles, *Journal of Geotechnical Engineering*, 1993, **119**, 91-107, doi: 10.1061/(asce)0733-9410(1993)119: 1(91).

[21] A. Izadi, R. Jamshidi Chenari, Three-dimensional finite-element lower bound solutions for lateral limit load of piles embedded in cross-anisotropic clay deposits, *International Journal of Geomechanics*, 2021, **21**, doi: 10.1061/(asce)gm.1943-5622.0002208.

[22] A. Izadi, R. J. Chenari, Three-dimensional undrained bearing capacity analysis of laterally loaded pile in heterogeneous marine deposits, *Marine Georesources & Geotechnology*, 2022, **40**, 213-234, doi: 10.1080/1064119X.
2021.1881670.

[23] S. Keawsawasvong, B. Ukritchon, Ultimate lateral capacity of two-dimensional plane strain rectangular pile in clay, *Geomechanics and Engineering*, 2016, **11**, 235-252, doi: 10.12989/gae.2016.11.2.235.

[24] S. Keawsawasvong, B. Ukritchon, Undrained lateral capacity of I-shaped concrete piles, *Songklanakarin Journal of Science and Technology*, 2017, **39**, 751-758.

[25] B. Ukritchon, S. Keawsawasvong, Undrained lateral capacity of rectangular piles under a general loading direction and full flow mechanism, *KSCE Journal of Civil Engineering*, 2018, **22**, 2256-2265, doi: 10.1007/s12205-017-0062-7.

[26] S. Keawsawasvong, W. Chaonoi, J. T. Chavda, L. Z. Mase, R. Banyong, Undrained lateral resistance of fixed-headed rectangular and circular piles, *Transportation Infrastructure Geotechnology*, 2022, 1-16, doi: 10.1007/s40515-022-00260-4.

[27] S. Keawsawasvong and B. Ukritchon, Undrained capacity of laterally loaded underground walls subjected to horizontal load and moment, *Journal of GeoEngineering*, 2016, **11**, 75-83.

[28] S. Keawsawasvong, B. Ukritchon, Finite element analysis of undrained stability of cantilever flood walls, International Journal of Geotechnical Engineering, 2017, **11**, 355-367, doi: 10.1080/19386362.2016.1222044.

[29] S. Keawsawasvong, B. Ukritchon, Three-dimensional interaction diagram for the undrained capacity of inverted T-shape strip footings under general loading, *International Journal of Geotechnical Engineering*, 2018, **12**, 133-146, doi: 10.1080/19386362.2016.1252141.

[30] S. Keawsawasvong, B. Ukritchon, Failure modes of laterally loaded piles under combined horizontal load and moment considering overburden stress factors, *Geotechnical and Geological Engineering*, 2020, **38**, 4253-4267, doi: 10.1007/s10706-020-01293-7.

[31] S. Keawsawasvong, B. Ukritchon, Design equation for stability of a circular tunnel in anisotropic and heterogeneous clay, *Underground Space*, 2022, **7**, 76-93, doi: 10.1016/j.undsp.2021.05.003.

[32] B. Ukritchon, P. Wongtoythong, S. Keawsawasvong, New design equation for undrained pullout capacity of suction caissons considering combined effects of caisson aspect ratio, adhesion factor at interface, and linearly increasing strength, *Applied Ocean Research*, 2018, **75**, 1-14, doi: 10.1016/j.apor.2018.03.007.

[33] B. Ukritchon, S. Keawsawasvong, Unsafe error in conventional shape factor for shallow circular foundations in normally consolidated clays, *Journal of Geotechnical and Geoenvironmental Engineering*, 2017, **143**, 02817001, doi: 10.1061/(asce)gt.1943-5606.0001670.

[34] J. Shiau, B. Chudal, K. Mahalingasivam, S. Keawsawasvong, Pipeline burst-related ground stability in blowout condition, *Transportation Geotechnics*, 2021, **29**, 100587, doi: 10.1016/j.trgeo.2021.100587.

[35] S. Keawsawasvong, J. Shiau, C. Ngamkhanong, V. Qui Lai, C. Thongchom, Undrained stability of ring foundations: axisymmetry, anisotropy, and nonhomogeneity, *International Journal of Geomechanics*, 2022, **22**, 04021253, doi: 10.1061/(asce)gm.1943-5622.0002229.

[36] S. Keawsawasvong, B. Ukritchon, Undrained stability of a spherical cavity in cohesive soils using finite element limit analysis, *Journal of Rock Mechanics and Geotechnical Engineering*, 2019, **11**, 1274-1285, doi: 10.1016/j.jrmge.2019.07.001.

[37] W. Yodsomjai, S. Keawsawasvong, C. Thongchom, J. Lawongkerd, Undrained stability of unsupported conical slopes in two-layered clays, *Innovative Infrastructure Solutions*, 2020, **6**, 1-17, doi: 10.1007/s41062-020-00384-x.

[38] W. Chaonoi, J. Shiau, C. Ngamkhanong, C. Thongchom, P. Jamsawang, S. Keawsawasvong, Predicting lateral resistance of piles in cohesive soils, *Sustainability*, 2022, **14**, 12940, doi: 10.3390/su141912940.

